COMMUNICATION

Monodispersed Cu-TCPP/Cu_2O Hybrid Microspheres: A Superior Cascade Electrocatalyst Toward CO_2 Reduction to C_2 Products

Zi-Xuan Wan [a], Aidar Kuchkaev [b], Dmitry Yakhvarov [b,c,*], Xiong-Wu Kang [a,*]

[a] New Energy Research Institute, School of Environment and Energy, South China University of Technology, Higher Education Mega Center, Guangzhou, 510006, Guangdong, China
[b] Arbuzov Institute of Organic and Physical Chemistry, FRC Kazan Scientific Center of RAS, Arbuzov Street 8, Kazan, 420088, Russian Federation
[c] Alexander Butlerov Institute of Chemistry, Kazan Federal University, Kremlyovskaya Street 18, Kazan, 420008, Russian Federation

Abstract

The electrochemical conversion of carbon dioxide (CO_2) into valuable chemicals is a feasible way to mitigate the negative impacts of overmuch CO_2 emissions. Porphyrin-based metal organic frameworks (MOFs) are expected to be used for selective and efficient electrochemical CO_2 reduction (ECR) with porous structure and ordered active sites. Herein, we report the synthesis of a monodispersed and spherical organic/inorganic hybrid Cu-TCPP@Cu_2O electrocatalyst composed of Cu-TCPP (TCPP = tetrakis (4-carboxyphenyl) porphyrin) and Cu_2O, where TCPP plays significant roles in regulating the morphology. *In-situ* formed Cu during ECR process in combination with Cu-TCPP (Cu-TCPP@Cu) can suppress hydrogen evolution, enrich CO intermediate and promote C−C coupling toward C_2 products. The Cu-TCPP@Cu supported on porous carbon (PC) showed ultrafine Cu nanoclusters on PC, and displayed high ECR activity and selectivity toward C_2 products, with a C_2 faradaic efficiency of 62.3% at −1.0 V versus the reversible hydrogen electrode and a C_2 partial current density of 83.4 mA·cm^{-2}, which is 7.6 times and 13.1 times those of pure Cu_2O and TCPP, respectively. The morphology and hybrid structure of the catalyst were studied to improve the selectivity of ECR to produce C_2 products, which provides a new idea for the design of high-performance ECR catalyst.

Keywords: Organic/inorganic hybrid electrocatalysts; TCPP; Cuprous oxide; Cascade electrocatalysts

1. Introduction

Human activities lead to excessive emission of carbon dioxide (CO_2) into the atmosphere, resulting in serious environmental and climate problems, such as glacier melting and greenhouse effect [1−4]. Powerful methods of storing and converting CO_2 have been developed to reduce CO_2 levels in the atmosphere [5−8], among which, renewable energy driven electrocatalytic reduction of CO_2 (ECR) into valuable multi-carbon products is one of the promising and sustainable approaches [9−12]. However, catalysts limit the efficiency and selectivity of electrochemical CO_2 reduction [13−15]. Therefore, people have been committed to the development of a variety of efficient selective conversion of CO_2 electrocatalysts [16,17], like metal oxides [18,19], carbon-based materials [20] and metal organic frameworks (MOFs) [21,22]. Despite the significant progress, it remains a huge challenge to direct the reaction path to the ideal product, which requires the development of better electrocatalysts with higher product selectivity and catalytic activity [23−25].

MOF is regarded as an advantageous ECR electrocatalyst because of its porous crystalline

Received 7 April 2023; Received in revised form 15 May 2023; Accepted 7 June 2023
Available online 14 June 2023

* Corresponding author, Xiong-Wu Kang, Tel: (86-20)39381206, E-mail address: esxkang@scut.edu.cn.
* Corresponding author, Dmitry Yakhvarov, E-mail address: yakhvar@iopc.ru.

https://doi.org/10.13208/j.electrochem.2303271

structure and CO_2 affinities [26,27]. Therefore, a large number of molecular catalysts combining transition metal (TM) elements (like Fe, Co, Ni, Mn and Cu) with macrocyclic ligands (such as polypyridine, porphyrins and phthalocyanine) have been examined for the electrochemical reduction of CO_2 [28]. For instance, Chi and co-workers synthesized a kind of porous three-dimensional porphyrinic cobalt MOF with a CO faradaic efficiency of 92.4% at −0.6 V vs. reversible hydrogen electrode (RHE) [29]. In addition, Kongpatpanich [30] prevented the aggregation of porphyrins by embedding functionalized cobalt-based and iron-based porphyrins into rigid frame structures, and ensured that the H bond interface was only close to the intermediate products of ECR at the same time, thus reducing the limit potential of ECR and improving the selectivity of ECR. Besides, Su's team synthesized a series of structurally stable metallic two-dimensional (2D) polyoxometale-metalloporphyrin organic frameworks (TM-PMOFs, TM = Fe, Co, Ni, Cu, Zn, Ru, Rh, Pd, Os, Ir, Pt). Their calculations showed that Lindqvist type clusters $[Mo_6]^{2e/2H}$ can act as a multi-electron regulator of the reduction reaction, reducing the drive potential of the reaction (0.08 V) [31]. Unfortunately, considering the completion of the multi-electron transfer process required to obtain any reduced product in ECR, the poor conductivity and electron-donating capacity of MOF have always been a major limitation of MOF as an efficient electrocatalyst [32]. Therefore, it is imperative to design a novel catalyst with active components, electron-rich units and electron mobility.

At present, metals [33−35], metal sulfides [36], organic groups [37] and metal oxides [38−40] have been combined with porphyrin complexes to improve their activity and produce synergistic effects. Tetrakis (4-carboxyphenyl) porphyrin (TCPP) is a kind of electron donor which has been used to improve the ECR performances of MOFs [41]. Electron transfer could be facilitated by integrating electron-rich units into porphyrin-based MOFs, which could obtain excellent ECR activity. For example, Chang and colleagues reported a urea pendant modified molecular iron porphyrin catalyst with high CO faradaic efficiency, and the catalytic rate was 1500 times that of the unmodified parent iron porphyrin [42].

In addition, Zheng's group also developed a donor-acceptor modified Cu porphyrin (Cu-TAPP), which exhibited an excellent CO_2-to-CH_4 electroreduction performance, including a high CH_4 partial current density of 290.5 $mA \cdot cm^{-2}$ and a corresponding faradaic efficiency of 54.8% at −1.63 V vs. RHE in flow cells [43]. Liang's team [44] also synthesized nickel phthalocyanine (NiPc-MDE) with methoxy (−OMe) and cyanide (−CN). Compared with cyano-substituted NiPC-CN-MDE, the methoxy-substituted NiPC-OMe-MDE catalyst can stabilize *COOH intermediates and improve the selectivity of CO. The NiPC−OMe-MDE catalyst could maintain 99.5% CO selectivity in the current density range of 10−300 $mA \cdot cm^{-2}$. Although these materials can effectively promote the catalysis of electrochemical reduction of CO_2, the ECR C_2 products are still very limited. Promoting the multi-electron transfer reactions with high selectivity of C_2 products remains a grand challenge for molecular-based electrocatalysts.

Herein, we report the deliberate synthesis of monodispersed and spherical organic/inorganic hybrid Cu-TCPP@Cu_2O, composed of 2-dimentional Cu-TCPP and Cu_2O, which can be converted to Cu-TCPP@Cu during the ECR process and displays a faradaic efficiency of 62.3% at −1.0 V vs. RHE. Our study shows that the interaction between Cu-TCPP and Cu_2O is the key factor contributing to its excellent ECR performance.

2. Experimental section

2.1. Materials

Tetrakis (4-carboxyphenyl) porphyrin (TCPP, 97%), zinc nitrate hexahydrate ($Zn(NO_3)_2 \cdot 6H_2O$, 98%), trifluoroacetic acid (99%) and copper nitrate trihydrate ($Cu(NO_3)_2 \cdot 3H_2O$, 99%) were purchased from Macklin. N, N-dimethylformamide (DMF, 99.9%), methanol, ethanol, 2-methylimidazole, potassium hydroxide (KOH, 95%) and polyvinylpyrrolidone (PVP, average mol·wt. 50,000) were purchased from Energy Chemical Co. Deionized water (DI, 18.2 MΩ·cm) was acquired from Milli-Q system. All agents were analytically pure and used without further purification.

2.2. Preparations of Cu-TCPP@Cu_2O and contrastive samples

2.2.1. Synthesis of Cu-TCPP@Cu_2O nanoparticles

A solution made of TCPP (20 mg, 0.025 mmol) and PVP (500 mg) in DMF (16 mL) was added to a solution of $Cu(NO_3)_2 \cdot 3H_2O$ (121.91 mg, 0.65 mmol) in DMF (10 mL). The mixed solution was refluxed for 24 h at 120 °C after stirring for 2 min [45]. After cooling down to room temperature, the resulting red Cu-TCPP@Cu_2O nanoparticles were washed four times with DI water and collected by centrifuging at 8500 rpm for 5 minutes.

The synthesis process of pure Cu_2O was the same as that of Cu-TCPP@Cu_2O without TCPP.

The synthesis process of pure Cu-TCPP was the same as that of Cu-TCPP@Cu_2O except for the addition of trifluoroacetic acid (20 μL, 1.0 mol·L^{-1}).

In addition, the catalysts after ECR corresponding to Cu-TCPP@Cu_2O, Cu_2O, Cu-TCPP and TCPP are named as Cu-TCPP@Cu, OD-Cu, Cu-TCPP spent and TCPP spent, respectively, while the corresponding samples mixed with porous carbon (PC) are named as Cu-TCPP@Cu_2O/PC, Cu_2O/PC, Cu-TCPP/PC and TCPP/PC.

2.2.2. Synthesis of porous carbon by carbonization of ZIF-8

The $Zn(NO_3)_2 \cdot 6H_2O$ (5.94 g, 0.02 mol) and 2-methylimidazole (6.56 g, 0.08 mol) were added into methanol (500 mL). After mixing for 12 h at room temperature, the formed ZIF-8 nanoparticles were washed for three times with methanol and collected by centrifuging at 8500 rpm for 3 minutes.

The ZIF-8 (500 mg) was put at a porcelain boat in a quartz tube furnace. Subsequently, the temperature of the tube furnace was elevated to 950 °C with a heating rate of 5 °C·min^{-1} under Ar atmosphere and held at this temperature for 3 h. The obtained porous carbon is named as PC.

2.3. Morphological and structural characterizations

Powder X-ray diffraction (Bruker D8 Advanced, German) test was performed using a Cu K_α radiation source. X-ray photoelectron spectroscopic (XPS) measurements were performed on a PHI X-tool X-ray photoelectron spectrometer using Al as the exciting source. Scanning electron microscopic (SEM) images and the elements distribution of the catalyst were recorded using a Zeiss Supra 55. Transmission electron microscopic (TEM) images were obtained on a Talos F200x.

2.4. Electrochemical characterization

Electrochemical CO_2 reduction tests were performed on a CHI 660E electrochemical analyzer using a designed gas-tight flow cell. None of the electrochemical tests in this work used IR compensation. The platinum foil counter electrode was purchased from Sigma Aldrich. The Hg/HgO reference electrode and carbon fiber paper were purchased from Gaoss Union. The conversion of the Hg/HgO electrode to the reversible hydrogen electrode (RHE) is performed using the following formula [46]:

$$E_{RHE} = E_{Hg/HgO} + 0.095\ V + 0.059 \times pH$$

Firstly, a diluted Nafion solution was prepared by mixing 5 mL DI water, 5 mL ethanol and 0.5 mL Nafion solution (5% *w*/*w*). Disperse 2.5 mg of Cu-TCPP@Cu_2O catalyst and 2.5 mg PC into 5 mL of the diluted Nafion solution, by sonication for 30 min to obtain a catalyst ink. Drop-cast 1 mL the catalyst ink onto each carbon paper with gas diffusion layer (GDL) to obtain the catalyst-loaded gas diffusion electrode (GDE, 2 cm × 0.5 cm). The geometric area of each electrode is 1 cm^2 and the catalyst loading on each electrode was controlled to be 1.0 mg·cm^{-2}. The working electrodes for pristine Cu_2O/PC, Cu-TCPP/PC and TCPP/PC were prepared by following the same procedure as that of Cu-TCPP@Cu_2O/PC.

For all experiments, 1.0 mol·L^{-1} KOH (pH = 14) solution was used as the electrolyte. The durability was evaluated by chronoamperometric profiles at a constant current density. The double-layer capacitance (C_{dl}) values and electrochemical surface area (ECSA) were determined by cyclic voltammetric (CV) curves at different scanning rates. Electrochemical impedance spectroscopic (EIS) measurements were made at frequencies ranging from 100 kHz to 0.01 Hz in a potentiostatic mode. Current densities were calculated based on the catalyst-covered geometric area of the working electrode. All potentials reported in this work are referred to RHE. The liquid product of ECR was quantified by ^1H NMR spectra recorded with an Agilent 400 MHz NMR instrument. The gas product generation of ECR was calculated by gas chromatography with an HuaAi GC-9560.

3. Results and discussion

The morphology of Cu-TCPP@Cu_2O was examined by SEM and TEM. In Fig. 1a, Cu-TCPP@Cu_2O exhibits a spherical shape and a bumpy surface, with a size of 2.78 ± 0.67 μm in diameter (Fig. S1a–b). It is highly possible that the bumpy surface of Cu-TCPP@Cu_2O was assembled with ultrathin nanosheet of Cu-TCPP [47]. The element mapping for Cu-TCPP@Cu_2O demonstrates the uniform distribution of each element on the sample. The high-resolution TEM image of Cu-TCPP@Cu_2O (Fig. 1b) further indicates the rough surface, composed of small nanoparticles at 3–5 nanometres. The lattice fringe at the heart of the sample was identified to be 0.2464 nm (Fig. 1c), which agrees with Cu_2O (1 1 1) reflection [47]. Similarly, the pristine Cu_2O sample without TCPP functionalization equally shows spherical shape, and two-size distribution in diameter, i.e., 96.56 and 264.74 nm, which are much smaller than that of Cu-TCPP@Cu (Fig. 1d and Fig. S2a–c). This indicates that TCPP plays significant roles in regulating the morphology of Cu_2O.

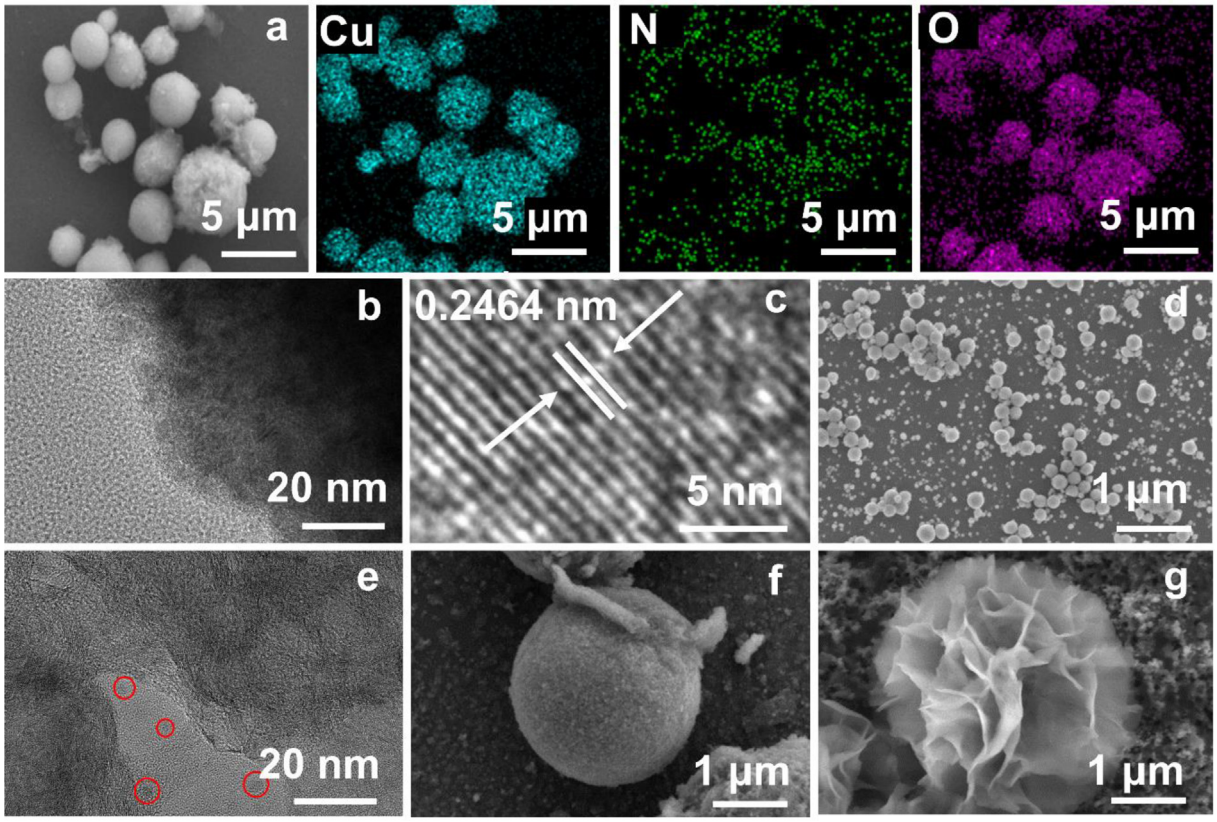

Fig. 1. The structural characterization: (a) SEM image of the Cu-TCPP@Cu_2O and the corresponding EDX mapping images of Cu, N, O, (b—c) TEM images of Cu-TCPP@Cu_2O and (d) SEM image of Cu_2O, (e) TEM image of Cu-TCPP@Cu/PC, (f) SEM image of Cu-TCPP@Cu and (g) SEM image of Cu-TCPP.

After an electrolysis at −1.0 V for 30 min, the Cu_2O nanoparticles were converted to metallic Cu, and the Cu nanoclusters with a diameter of about 3 nm on PC were observed for the Cu-TCPP@Cu/PC sample (Fig. 1e). Fig. 1f indicates that Cu-TCPP@Cu_2O retains its spherical structure even after the electrolysis. In contrast, the highly porous and aggregated Cu nanoparticles and nanowires at hundreds of nanometre scale were observed for the pure Cu_2O after the electrolysis (OD-Cu, Fig S3a—3b). Apparently, Cu-TCPP can modulate not only the growth dynamics of Cu_2O, but also the recrystallization process of Cu during ECR process when Cu_2O is converted to Cu. Due to the strong interaction of Cu-TCPP and Cu, the structure of Cu-TCPP@Cu_2O was mainly maintained. SEM observation of Cu-TCPP fresh and Cu-TCPP spent (Figs. 1g and 3c—3d) also proves its structural stability. Cu-TCPP displays a nanoflower-like structure. After the electrolysis, the structure collapsed slightly but still maintained a flower-like structure in general. In Fig. S3e—3f, TCPP shows a severe aggregation both before and after the electrolysis.

As shown in Fig. 2 and Fig. S4, the peaks at 2θ values of 7.96, 11.03, 19.0 and 22.02° could be indexed to (110), (200), (004) and (400) reflection

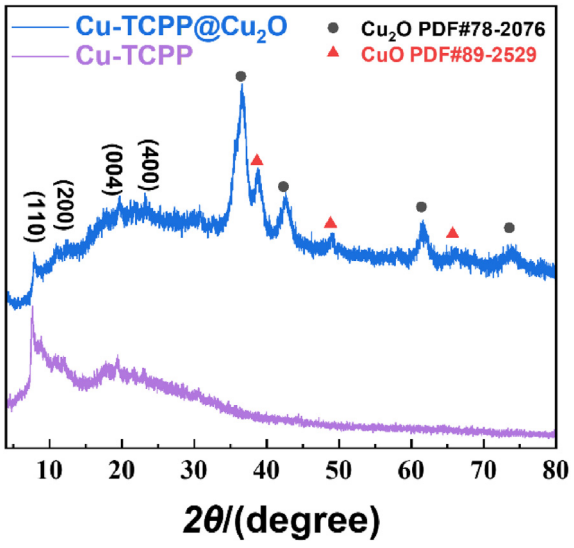

Fig. 2. XRD patterns of Cu-TCPP@Cu_2O and Cu-TCPP.

[47—50] of Cu-TCPP MOF, respectively, in Cu-TCPP@Cu_2O and Cu-TCPP both before and after the electrolysis. The peaks at 36.52, 42.32, 61.43 and 73.34° correspond to the crystal planes of (111), (200), (220) and (311) of crystalline Cu_2O, respectively [51], which are observed for both

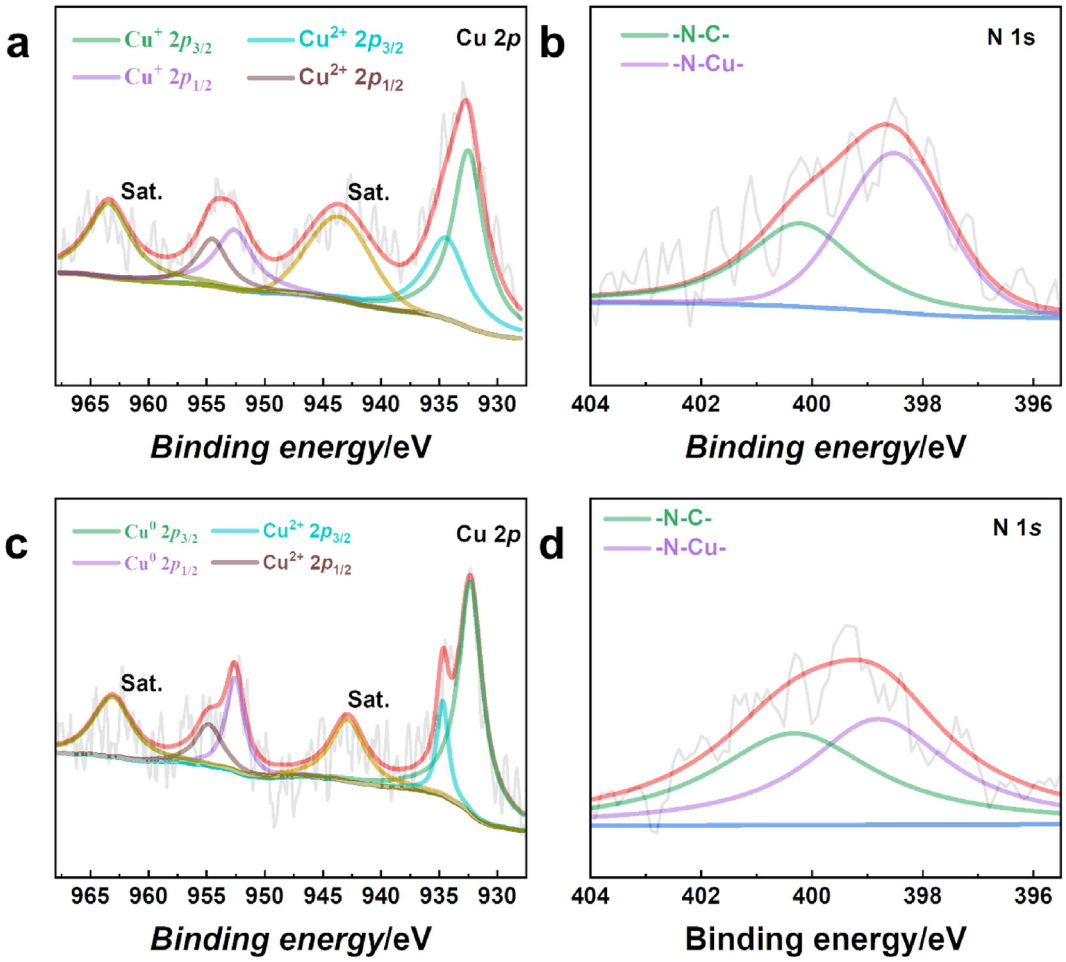

Fig. 3. XPS spectra of (a) Cu 2p, (b) N 1s for Cu-TCPP@Cu_2O/PC and (c) Cu 2p, (d) N 1s for Cu-TCPP@Cu/PC.

Cu-TCPP@Cu_2O and Cu_2O. In addition, the small peaks at 38.77, 48.84 and 65.73° might be indexed to CuO (PDF#89-2529).

Cu^{2+} may possibly not be completely converted into Cu^+ during the preparation of catalyst, thus a small amount of CuO was remained in the catalyst. However, Cu_2O could still be dominant in the Cu-TCPP@Cu_2O. The XRD results indicate that the Cu-TCPP@Cu_2O represented the Cu-TCPP functionalized Cu_2O, while only the pure phase of Cu_2O was obtained without using TCPP in the synthetic procedure. After an electrolysis at −1.0 V, the characteristic peak of Cu_2O vanished from both Cu-TCPP@Cu_2O and Cu_2O, and only those diffraction peaks related to Cu were observed, signifying the complete conversion of Cu_2O to Cu at the ECR process. However, the diffraction peaks of Cu-TCPP were well maintained during the electrolysis, indicating its high stability against ECR process.

As shown in Fig. 2 and Fig. S4, the peaks at 2θ values of 7.96, 11.03, 19.0 and 22.02° could be indexed to (110), (200), (004) and (400) reflection [47−50] of Cu-TCPP MOF, respectively, in Cu-TCPP@Cu_2O and Cu-TCPP both before and after the electrolysis. The peaks at 36.52, 42.32, 61.43 and 73.34° correspond to the crystal planes of (111), (200), (220) and (311) of crystalline Cu_2O, respectively [51], which are observed for both Cu-TCPP@Cu_2O and Cu_2O. In addition, the small peaks at 38.77, 48.84 and 65.73° might be indexed to CuO (PDF#89−2529).

Cu^{2+} may possibly not be completely converted into Cu^+ during the preparation of catalyst, thus a small amount of CuO was remained in the catalyst. However, Cu_2O could still be dominant in the Cu-TCPP@Cu_2O. The XRD results indicate that the Cu-TCPP@Cu_2O represented the Cu-TCPP functionalized Cu_2O, while only the pure phase of Cu_2O was obtained without using TCPP in the synthetic procedure. After an electrolysis at −1.0 V, the characteristic peak of Cu_2O vanished from both Cu-TCPP@Cu_2O and Cu_2O, and only those diffraction peaks related to Cu were observed, signifying the complete conversion of Cu_2O to Cu at the ECR process. However, the diffraction peaks of Cu-TCPP were well maintained during the electrolysis, indicating its high stability against ECR process.

Fig. 3a shows the Cu 2*p* spectrum for the as-prepared Cu-TCPP@Cu_2O. The binding energies at 932.5, 934.7 and 943.9 eV were assigned to Cu^{1+} in Cu_2O, Cu^{2+} in CuO and Cu-TCPP, and the satellite of a Cu $2p_{3/2}$ peak, respectively [52,53]. Three peaks appeared at 952.4, 954.6, and 963.4 eV were attributed to Cu^{+} in Cu_2O, Cu^{2+} in CuO and Cu-TCPP, and the satellite of a Cu $2p_{1/2}$ peak, respectively [45,52,53]. In Fig. 3b, the N 1*s* spectra of Cu-TCPP@Cu_2O/PC observed at 400.3 eV and 398.8 eV could be accounted for pyridinic−N and Cu−N bond, respectively [50]. This further indicates the presence of Cu-TCPP in Cu-TCPP@Cu_2O composite. As shown in Fig. 3c, after the electrolysis, the satellite peak of Cu remained, which may come from Cu^{2+} species in Cu-TCPP [50]. This further confirms the integrity of Cu-TCPP against ECR electrolysis.

It should also be noted that the intensity of the Cu oxide satellite peak becomes much weaker than that of the fresh sample due to the conversion of Cu_2O to Cu. The binding energies at 932.5 and 934.7 eV were assigned to Cu^0 and a few Cu^{2+} in the Cu-TCPP (a Cu $2p_{3/2}$ peak) [52−54]. Two peaks appeared at 952.4 and 954.6 eV were attributed to Cu^0 and a few Cu^{2+} in the Cu-TCPP (a Cu $2p_{1/2}$ peak) [43]. In Fig. 3d, the N 1*s* spectra of Cu-TCPP@Cu exhibit a higher peak intensity of pyridinic−N and a lower peak intensity of Cu−N bond than those of Cu-TCPP@Cu_2O, possibly due to the partial breakage of Cu−N bond in Cu-TCPP, and conversion to metallic Cu and TCPP [55−57]. However, according to the XRD and SEM results, the Cu-TCPP structure in Cu-TCPP@Cu_2O can generally remain stable after the electrolysis.

The LSV (Fig. 4a) curves were recorded in N_2 and CO_2 atmospheres in 1.0 mol·L^{-1} KOH from 0 to −1.6 V. The current density of Cu-TCPP@Cu_2O/PC in CO_2 was higher than that in N_2, which indicates that the catalyst does have ECR activity. It was found that the products distribution of ECR over TCPP@Cu_2O/PC depends on the electrode potential (Fig. 4b). At −0.8 V and −0.9 V, C_1 product and H_2 became dominated in ECR. As the catalyst electrode was further negatively polarized to −1.0 V, the yields of ethanol and ethylene were dramatically increased, with ethylene being the dominant ECR product (Fig. 4b). C_2 product was the predominant ECR product for the Cu-TCPP@Cu_2O/PC catalyst at −1.0 V (Fig. 4b) and its FE reached 62.3%. In contrast, ECR was dominated by HER and CO on Cu_2O/PC (Fig. 4c), Cu-TCPP/PC (Fig. S5a) and TCPP/PC (Fig. S5b and Fig. S5c). These results indicate that the combination of Cu_2O and Cu-TCPP on PC is essential for efficient production of C_2 products in ECR.

In Fig. 4d, Cu-TCPP@Cu_2O/PC displays a supreme partial current density of C_2 products in the potential range of −0.8 V to −1.0 V, which is as high as 83.4 mA·cm^{-2} and more than 7.6 times those of the unmodified Cu_2O, Cu-TCPP and TCPP. As shown in Fig. S5d and Fig. S6, the partial current density of C_1 (which is mainly CO) on Cu-TCPP@Cu_2O/PC was comparable to those of

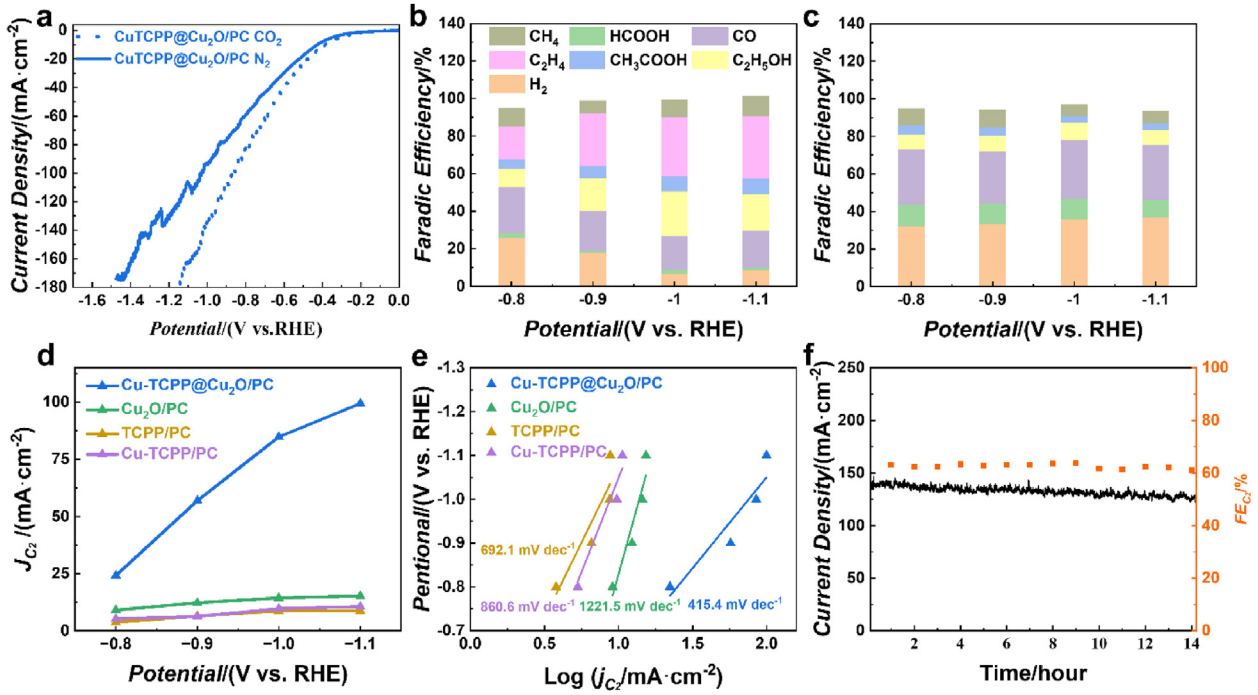

Fig. 4. ECR performance: (a) LSV of Cu-TCPP@Cu_2O/PC in CO_2 and N_2. Faradaic efficiencies for ECR products on (b) Cu-TCPP@Cu_2O/PC and (c) Cu_2O/PC across a potential range from −0.8 to −1.1 V vs. RHE, (d) Partial current density of C_2 and (e) Tafel plots for C_2 product of ECR on Cu-TCPP@Cu_2O/PC, Cu_2O/PC, Cu-TCPP/PC and TCPP/PC, respectively. (f) ECR stability assessment on Cu-TCPP@Cu_2O/PC at −1.0 V vs. RHE.

Cu_2O/PC and Cu-TCPP/PC but higher than TCPP/PC. It is further proved that the higher selectivity of C_2 product on Cu-TCPP@Cu_2O/PC can be obtained by C−C coupling of a large number of CO intermediates on Cu_2O/PC and Cu-TCPP/PC. Tafel slopes are calculated based on Tafel equation ($\eta = b \log j + a$, where η is the overpotential, j is the current density and b is the Tafel slope) [32] to elucidate the dynamics activity of catalyst for ECR (Fig. 4e). The Tafel slope for C_2 product on Cu-TCPP@Cu_2O/PC is 415.4 $mV \cdot dec^{-1}$, which is much smaller than those of Cu_2O/PC (1221.5 $mV \cdot dec^{-1}$), Cu-TCPP/PC (860.6 $mV \cdot dec^{-1}$) and TCPP/PC (692.1 $mV \cdot dec^{-1}$). The result states the favorable kinetics of Cu-TCPP@Cu_2O/PC for the formation of C_2 products.

It is highly possible that functionalization of OD-Cu with Cu-TCPP may enhance the hydrophobic properties of the catalyst composite, thus, suppressing the HER process. Additionally, both OD-Cu and Cu-TCPP here are good ECR catalysts for CO production, and the combination of Cu-TCPP and OD-Cu possibly enhances the local concentration of CO intermediates on OD-Cu surface, thus, promoting C−C coupling for C_2 production. According to earlier report [58,59], CO on Cu (2+) in Cu-TCPP and Cu (0) is also favorable to C−C coupling. All the three factors concurrently promote C_2 product in ECR process on Cu-TCPP@Cu_2O/PC catalyst. To examine the intrinsic activity of the catalysts, the electrochemical active surface area (ECSA) was evaluated by electrochemical double-layer capacitance (C_{dl}). Fig. S7−8 and Table S1 show that Cu-TCPP@Cu_2O/PC indeed exhibits larger C_{dl} value and ECSA than those of Cu_2O/PC, Cu-TCPP/PC and TCPP/PC, which provide more active sites in electrocatalyst to contact the electrolyte for ECR [29]. As shown in Fig. S9, the current density normalized to ECSA shows basically the same trend as in the geometric current density.

The Nyquist plots (Fig. S10) prove that Cu-TCPP@Cu_2O/PC has much smaller charge transfer resistance than Cu_2O/PC, Cu-TCPP/PC and TCPP/PC at the process of ECR, which indicates that Cu-TCPP@Cu_2O/PC can provide faster electron transfer from the catalyst surface to the reactant in intermediate generation, eventually resulting in largely enhanced activity and selectivity [60,61]. As shown in Fig. 4f, the faradaic efficiency of C_2 product is nearly 60% within 14 h at a potential of −1.0 V, indicating an outstanding ECR stability.

4. Conclusions

In this work, we have successfully prepared the uniformly distributed and spherical shaped Cu-TCPP@Cu_2O organic/inorganic hybrid catalyst, which is composed of 2-dimensional Cu-TCPP ultrathin nanosheet and Cu_2O. It shows the excellent ECR performance toward production of C_2 products, with a faradaic efficiency of 62.3% at a flow cell in 1.0 $mol \cdot L^{-1}$ KOH electrolyte. The Cu-TCPP@Cu_2O/PC catalyst had an inseparable interaction, which can effectively adsorb the intermediates, promoting the C−C coupling reaction and then improving the selectivity of C_2 products. This work highlights an effective strategy to design efficient Cu porphyrin-based MOF catalysts for electrochemical reduction of CO_2 into C_2 products.

Conflict of interest

There are no conflicts to declare.

Acknowledgements

This work was supported by the National Natural Science Foundation of China (No. U2032151).

References

[1] Wang W, Shang L, Chang G L, Yan C Y, Shi R, Zhao Y X, Waterhouse G IN, Yang D J, Zhang T R. Intrinsic carbon-defect-driven electrocatalytic reduction of carbon dioxide [J]. Adv. Mater., 2019, 31(19): 1808276.

[2] Luo T, Liu K, Fu J, Chen S, Li H, Pan H, Liu M. Electric double layer structure in electrocatalytic carbon dioxide reduction[J]. AESR, 2022, 4(3): 2200148.

[3] Mu Z Y, Han N, Xu D, Tian B L, Wang F Y, Wang Y Q, Sun Y M, Liu C, Zhang P K, Wu X J, Li Y G, Ding M N. Critical role of hydrogen sorption kinetics in electrocatalytic CO_2 reduction revealed by on-chip *in situ* transport investigations[J]. Nat. Commun., 2022, 13(1): 6911.

[4] Faunce T A, Lubitz W, Rutherford A W, MacFarlane D, Moore G F, Yang P, Nocera D G, Moore T A, Gregory D H, Fukuzumi S, Yoon K B, Armstrong F A, Wasielewski M R, Styring S. Energy and environment policy case for a global project on artificial photosynthesis[J]. Energy Environ. Sci., 2013, 6(3): 695−698.

[5] Masel R I, Liu Z, Yang H, Kaczur J J, Carrillo D, Ren S, Salvatore D, Berlinguette C P. An industrial perspective on catalysts for low-temperature CO_2 electrolysis[J]. Nat. Nanotechnol., 2021, 16(2): 118−128.

[6] Zhou Y J, Ni G H, Wu K Z, Chen Q, Wang X Q, Zhu W W, He Z, Li H M, Fu J W, Liu M. Porous Zn conformal coating on dendritic-like Ag with enhanced selectivity and stability for CO_2 electroreduction to CO[J]. Adv. Sustain. Syst., 2023, 7(1): 2200374.

[7] De Luna P, Quintero-Bermudez R, Dinh C T, Ross M B, Bushuyev O S, Todorović P, Regier T, Kelley S O, Yang P, Sargent E H. Catalyst electro-redeposition controls morphology and oxidation state for selective carbon dioxide reduction[J]. Nat. Catal., 2018, 1(2): 103−110.

[8] Pan B B, Fan J, Zhang J, Luo Y Q, Shen C, Wang C Q, Wang Y H, Li Y G. Close to 90% Single-pass conversion efficiency for CO_2 electroreduction in an acid-fed membrane electrode assembly[J]. ACS Energy Lett., 2022, 7(12): 4224−4231.

[9] Wu Y S, Jiang Z, Lu X, Liang Y Y, Wang H L. Domino electroreduction of CO_2 to methanol on a molecular catalyst[J]. Nature, 2019, 575(7784): 639−642.
[10] Wang Q, Liu K, Hu K, Cai C, Li H, Li H, Herran M, Lu Y R, Chan T S, Ma C, Fu J, Zhang S, Liang Y, Cortés E, Liu M. Attenuating metal-substrate conjugation in atomically dispersed nickel catalysts for electroreduction of CO_2 to CO[J]. Nat. Commun., 2022, 13(1): 6082.
[11] Zhao S L, Yang Y C, Tang Z Y. Insight into structural evolution, active sites, and stability of heterogeneous electrocatalysts[J]. Angew. Chem. Int. Ed., 2022, 61(11): e202110186.
[12] Liu P X, Peng L W, He R N, Li L L, Qiao J L. A high-performance continuous-flow MEA reactor for electroreduction CO_2 to formate[J]. J. Electrochem., 2022, 28(1): 2104231.
[13] Wang Y R, Yang R X, Chen Y, Gao G K, Wang Y J, Li S L, Lan Y Q. Chloroplast-like porous bismuth-based core-shell structure for high energy efficiency CO_2 electroreduction [J]. Sci. Bull., 2020, 65(19): 1635−1642.
[14] Tan D X, Cui C N, Shi J B, Luo Z X, Zhang B X, Tan X N, Han B X, Zheng L R, Zhang J, Zhang J L. Nitrogen-carbon layer coated nickel nanoparticles for efficient electrocatalytic reduction of carbon dioxide[J]. Nano Res., 2019, 12(5): 1167−1172.
[15] Hori Y, Wakebe H, Tsukamoto T, Koga O. Electrocatalytic process of Co selectivity in electrochemical reduction of CO_2 at metal electrodes in aqueous media[J]. Electrochim. Acta, 1994, 39(11): 1833−1839.
[16] Deng P L, Yang F, Wang Z T, Chen S H, Zhou Y Z, Zaman S, Xia B Y. Metal-organic framework-derived carbon nanorods encapsulating bismuth oxides for rapid and selective CO_2 electroreduction to formate[J]. Angew. Chem. In. Ed., 2020, 59(27): 10807−10813.
[17] Li Q, Fu J J, Zhu W L, Chen Z Z, Shen B, Wu L H, Xi Z, Wang T Y, Lu G, Zhu J J, Sun S H. Tuning Sn-catalysis for electrochemical reduction of CO_2 to CO via the core/shell Cu/SnO_2 structure[J]. J. Am. Chem. Soc., 2017, 139(12): 4290−4293.
[18] Gao S, Lin Y, Jiao X C, Sun Y F, Luo Q Q, Zhang W H, Li D Q, Yang J L, Xie Y. Partially oxidized atomic cobalt layers for carbon dioxide electroreduction to liquid fuel[J]. Nature, 2016, 529(7584): 68−71.
[19] Zhang L, Zhao Z J, Gong J. Nanostructured materials for heterogeneous electrocatalytic CO_2 reduction and their related reaction mechanisms[J]. Angew. Chem. Int. Ed., 2017, 56(38): 11326−11353.
[20] Han S G, Ma D D, Zhu Q L. Atomically structural regulations of carbon-based single-atom catalysts for electrochemical CO_2 reduction[J]. Small Methods, 2021, 5(8): 2100102.
[21] Du D Y, Qin J S, Li S L, Su Z M, Lan Y Q. Recent advances in porous polyoxometalate-based metal-organic framework materials[J]. Chem. Soc. Rev., 2014, 43(13): 4615−4632.
[22] Qin J S, Du D Y, Guan W, Bo X J, Li Y F, Guo L P, Su Z M, Wang Y Y, Lan Y Q, Zhou H C. Ultrastable polymolybdate-based metal-organic frameworks as highly active electrocatalysts for hydrogen generation from water[J]. J. Am. Chem. Soc., 2015, 137(22): 7169−7177.
[23] Peng C, Zhu X, Xu Z, Yan S, Chang L Y, Wang Z, Zhang J, Chen M, Sham T K, Li Y, Zheng G. Lithium vacancy-tuned [CuO_4] sites for selective CO_2 electroreduction to C_{2+} products[J]. Small, 2022, 18(8): 2106433.
[24] Guo Q, Fu J L, Zhang C Y, Cai C Y, Wang C, Zhou L H, Xu R B, Wang M Y. Preparation of CoO/RGO@Ni foam electrode and its electrocatalytic reduction of CO_2[J]. J. Electrochem., 2021, 27(4): 449−455.
[25] Zhu C, Chen W, Song Y F, Dong X, Li G H, Wei W, Sun Y H. Effect of reaction conditions on Cu-catalyzed CO_2 electroreduction[J]. J. Electrochem., 2020, 26(6): 797−807.
[26] Liang Z B, Qu C, Guo W H, Zou R Q, Xu Q. Pristine metal-organic frameworks and their composites for energy storage and conversion[J]. Adv. Mater., 2018, 30(37): 1702891.
[27] Kornienko N, Zhao Y, Kley C S, Zhu C, Kim D, Lin S, Chang C J, Yaghi O M, Yang P. Metal-organic frameworks for electrocatalytic reduction of carbon dioxide[J]. J. Am. Chem. Soc., 2015, 137(44): 14129−14135.
[28] Savéant J M. Molecular catalysis of electrochemical reactions. Mechanistic aspects[J]. Chem. Rev., 2008, 108(7): 2348−2378.
[29] Chi S Y, Chen Q, Zhao S S, Si D H, Wu Q J, Huang Y B, Cao R. Three-dimensional porphyrinic covalent organic frameworks for highly efficient electroreduction of carbon dioxide[J]. J. Mater. Chem. A, 2022, 10(9): 4653−4659.
[30] Wannakao S AO, Jumpathong W, Kongpatpanich K AO. Tailoring metalloporphyrin frameworks for an efficient carbon dioxide electroreduction: Selectively stabilizing key intermediates with H-bonding pockets[J]. Inorg. Chem., 2017, 56(12): 7200−7209.
[31] Wang C, Zhu C Y, Zhang M, Geng Y, Li Y G, Su Z M. An intriguing window opened by a metallic two-dimensional lindqvist-cobaltporphyrin organic framework as an electrochemical catalyst for the CO_2 reduction reaction[J]. J. Mater. Chem. A, 2020, 8(29): 14807−14814.
[32] Wang Y R, Huang Q, He C T, Chen Y, Liu J, Shen F C, Lan Y Q. Oriented electron transmission in polyoxometalate-metalloporphyrin organic framework for highly selective electroreduction of CO_2[J]. Nat. Commun., 2018, 9(1): 4466.
[33] Hod I, Sampson M D, Deria P, Kubiak C P, Farha O K, Hupp J T. Fe-porphyrin-based metal-organic framework films as high-surface concentration, heterogeneous catalysts for electrochemical reduction of CO_2[J]. ACS Catal., 2015, 5(11): 6302−6309.
[34] Titi H M, Patra R, Goldberg I. Exploring supramolecular self-assembly of tetraarylporphyrins by halogen bonding: Crystal engineering with diversely functionalized six-coordinate tin(L)$_2$-porphyrin tectons[J]. Chem. Eur J., 2013, 19(44): 14941−14949.
[35] Li J W, Zeng H L, Dong X, Ding Y M, Hu S P, Zhang R H, Dai Y Z, Cui P X, Xiao Z, Zhao D H, Zhou L J, Zheng T T, Xiao J P, Zeng J, Xia C. Selective CO_2 electrolysis to CO using isolated antimony alloyed copper[J]. Nat. Commun., 2023, 14(1): 340.
[36] He T, Chen S M, Ni B, Gong Y, Wu Z, Song L, Gu L, Hu W P, Wang X. Zirconium-porphyrin-based metal-organic framework hollow nanotubes for immobilization of noble-metal single atoms[J]. Angew. Chem. Int. Ed., 2018, 57(13): 3493−3498.
[37] Jin S, Son H J, Farha O K, Wiederrecht G P, Hupp J T. Energy transfer from quantum dots to metal-organic frameworks for enhanced light harvesting[J]. J. Am. Chem. Soc., 2013, 135(3): 955−958.
[38] Modak A, Nandi M, Mondal J, Bhaumik A. Porphyrin based porous organic polymers: Novel synthetic strategy and exceptionally high CO_2 adsorption capacity[J]. Chem. Commun., 2012, 48(2): 248−250.
[39] Liu C X, Zhang M L, Li J W, Xue W Q, Zheng T T, Xia C, Zeng J. Nanoconfinement engineering over hollow multi-shell structured copper towards efficient electrocatalytical C−C coupling[J]. Angew. Chem. Int. Ed., 2022, 61(3): e202113498.
[40] Teng X, Niu Y L, Gong S Q, Liu X, Chen Z F. Selective CO_2 reduction to formate on heterostructured Sn/SnO_2

nanoparticles promoted by carbon layer networks[J]. J. Electrochem., 2022, 28(2): 2108441.

[41] Gong L, Gao Y, Wang Y H, Chen B T, Yu B Q, Liu W B, Han B, Lin C X, Bian Y Z, Qi D D, Jiang J Z. Efficient electrocatalytic carbon dioxide reduction with tetraphenylethylene- and porphyrin-based covalent organic frameworks[J]. Catal. Sci. Technol., 2022, 12(21): 6566−6571.

[42] Derrick J S, Loipersberger M, Nistanaki S K, Rothweiler A V, Head-Gordon M, Nichols E M, Chang C J. Templating bicarbonate in the second coordination sphere enhances electrochemical CO_2 reduction catalyzed by iron porphyrins[J]. J. Am. Chem. Soc., 2022, 144(26): 11656−11663.

[43] Yu P E, Lv X M, Wang Q H, Huang H L, Weng W J, Peng C, Zhang L J, Zheng G F. Promoting electrocatalytic CO_2 reduction to CH_4 by copper porphyrin with donor-acceptor structures[J]. Small, 2022, 19(4): 2205730.

[44] Zhang X, Wang Y, Gu M, Wang M Y, Zhang Z S, Pan W Y, Jiang Z, Zheng H Z, Lucero M, Wang H L, Sterbinsky G E, Ma Q, Wang Y G, Feng Z X, Li J, Dai H J, Liang Y Y. Molecular engineering of dispersed nickel phthalocyanines on carbon nanotubes for selective CO_2 reduction[J]. Nat. Energy, 2020, 5(9): 684−692.

[45] Li B, Wang X Y, Chen L, Zhou Y L, Dang W T, Chang J, Wu C T. Ultrathin Cu-TCPP MOF nanosheets: A new theragnostic nanoplatform with magnetic resonance/near-infrared thermal imaging for synergistic phototherapy of cancers[J]. Theranostics, 2018, 8(15): 4086−4096.

[46] Feng L L, Yu G T, Wu Y Y, Li G D, Li H, Sun Y H, Asefa T, Chen W, Zou X X. High-index faceted Ni_3S_2 nanosheet arrays as highly active and ultrastable electrocatalysts for water splitting[J]. J. Am. Chem. Soc., 2015, 137(44): 14023−14026.

[47] Zhao M T, Wang Y X, Ma Q L, Huang Y, Zhang X, Ping J F, Zhang Z C, Lu Q P, Yu Y F, Xu H, Zhao Y L, Zhang H. Ultrathin 2D metal-organic framework nanosheets[J]. Adv. Mater., 2015, 27(45): 7372−7378.

[48] Li J, Song S, Meng J S, Tan L, Liu X M, Zheng Y F, Li Z Y, Yeung K WK, Cui Z D, Liang Y Q, Zhu S L, Zhang X C, Wu S L. 2D MOF periodontitis photodynamic ion therapy[J]. J. Am. Chem. Soc., 2021, 143(37): 15427−15439.

[49] La D D, Thi H PN, Kim Y S, Rananaware A, Bhosale S V. Facile fabrication of Cu(II)-porphyrin MOF thin films from tetrakis(4-carboxyphenyl)porphyrin and $Cu(OH)_2$ nanoneedle array[J]. Appl. Surf. Sci., 2017, 424: 145−150.

[50] Zhao S Y, Li S, Zhao Z C, Su Y P, Long Y K, Zheng Z Q, Cui D L, Liu Y, Wang C F, Zhang X J, Zhang Z T. Microwave-assisted hydrothermal assembly of 2d copper-porphyrin metal-organic frameworks for the removal of dyes and antibiotics from water[J]. Environ. Sci. Pollut. Res., 2020, 27(31): 39186−39197.

[51] Kooti M. Fabrication of nanosized cuprous oxide using Fehling's solution[J]. Transac. F: Nanotechnol., 2010, 17: 73.

[52] Karapinar D, Zitolo A, Huan T N, Zanna S, Taverna D, Galvão Tizei L H, Giaume D, Marcus P, Mougel V, Fontecave M. Carbon-nanotube-supported copper polyphthalocyanine for efficient and selective electrocatalytic CO_2 reduction to CO[J]. ChemSusChem, 2020, 13(1): 173−179.

[53] Xu T Y, Wei S T, Zhang X L, Zhang D T, Xu Y C, Cui X Q. Sulfur-doped Cu_3P|S electrocatalyst for hydrogen evolution reaction[J]. Mater. Res. Express, 2019, 6(7): 075501.

[54] Zhang J, Mao X N, Pan B B, Xu J, Ding X, Han N, Wang L, Wang Y H, Li Y G. Surface promotion of copper nanoparticles with alumina clusters derived from layered double hydroxide accelerates CO_2 reduction to ethylene in membrane electrode assemblies[J]. Nano Res., 2022, 16(4): 4685−4690.

[55] Mette G, Sutter D, Gurdal Y, Schnidrig S, Probst B, Iannuzzi M, Hutter J, Alberto R, Osterwalder J. From porphyrins to pyrphyrins: Adsorption study and metalation of a molecular catalyst on Au(111)[J]. Nanoscale, 2016, 8: 7958−7968.

[56] Mei B B, Liu C, Li J, Gu S Q, Du X L, Lu S Y, Song F, Xu W L, Jiang Z. Operando herfd-xanes and surface sensitive $\Delta\mu$ analyses identify the structural evolution of copper(II) phthalocyanine for electroreduction of CO_2[J]. J. Energy Chem., 2022, 64: 1−7.

[57] Tang J K, Zhu C Y, Jiang T W, Wei L, Wang H, Yu K, Yang C L, Zhang Y B, Chen C, Li Z T, Zhang D W, Zhang L M. Anion exchange-induced single-molecule dispersion of cobalt porphyrins in a cationic porous organic polymer for enhanced electrochemical CO_2 reduction via secondary-coordination sphere interactions[J]. J. Mater. Chem. A, 2020, 8(36): 18677−18686.

[58] Wang W, Deng C Y, Xie S J, Li Y F, Zhang W Y, Sheng H, Chen C C, Zhao J C. Photocatalytic C−C coupling from carbon dioxide reduction on copper oxide with mixed-valence copper(I)/copper(II)[J]. J. Am. Chem. Soc., 2021, 143(7): 2984−2993.

[59] Sang J Q, Wei P F, Liu T F, Lv H F, Ni X M, Gao D F, Zhang J W, Li H F, Zang Y P, Yang F, Liu Z, Wang G X, Bao X H. A reconstructed $Cu_2P_2O_7$ catalyst for selective CO_2 electroreduction to multicarbon products[J]. Angew. Chem. Int. Ed., 2022, 61(5): e202114238.

[60] Lin Z C, Jiang Z, Yuan Y B, Li H, Wang H X, Tang Y R, Liu C C, Liang Y Y. Cobalt-N_4 macrocyclic complexes for heterogeneous electrocatalysis of the CO_2 reduction reaction[J]. Chin. J. Catal., 2022, 43(1): 104−109.

[61] Siltamaki D, Chen S, Rahmati F, Lipkowski J, Cheng A C. Synthesis and electrochemical study of CuAu nanodendrites for CO_2 reduction[J]. J. Electrochem., 2021, 27(3): 278−290.

单分散 Cu-TCPP/Cu_2O 杂化微球:一种具有优异电还原 CO_2 产 C_2 性能的级联电催化剂

万紫轩 [a]，Aidar Kuchkaev[b]，Dmitry Yakhvarov[b,c,*]，康雄武 [a,*]
[a.]华南理工大学环境与能源学院新能源研究所，广东 广州 510006
[b] 阿尔布佐夫有机与物理化学研究所，俄罗斯联邦，喀山，420088
[c] 喀山联邦大学亚历山大·巴特列罗夫化学研究所，俄罗斯联邦，喀山，420008

摘要

高效电还原 CO_2（ECR）为有价值的多碳产物是解决 CO_2 排放问题的有效解决方案。基于卟啉的金属有机框架（MOFs）具有多孔结构和有序的活性位点，有望提高 ECR 生成多碳产物的选择性。本文制备了由铜-四（4-羧基）卟啉（Cu-TCPP）和 Cu_2O 组成的有机/无机杂化 Cu-TCPP@Cu_2O 电催化剂，其中 TCPP 在调控形貌方面起着重要作用。ECR 过程中原位形成的 Cu 与 Cu-TCPP（Cu-TCPP@Cu）结合可以抑制析氢，富集 CO 中间体，促进 C-C 偶联生成 C_2 产物。多孔碳（PC）负载的 Cu-TCPP@Cu 在 PC 上被还原为 Cu 纳米簇，同时对 C_2 产物具有较高的 ECR 活性和选择性。催化剂在–1.0 V 时（相对于可逆氢电极），C_2 产物法拉第效率为 62.3%，部分电流密度为 83.4 mA·cm^{-2}，是纯 Cu_2O 和 TCPP 的 7.6 倍和 13.1 倍。本论文研究了催化剂形貌和杂化结构如何提高 ECR 生 C_2 产物的选择性，为高性能 ECR 催化剂的设计提供了新思路。

关键字：有机/无机杂化电催化剂；四（4-羧基）卟啉；氧化亚铜；级联电催化剂